Research Article BEU Fen Bilimleri Dergisi 15(1): 86-96 (2026) DOI: 10.17798/bitlisfen.1757423

BİTLİS EREN UNIVERSITY
FEN BİLİMLERİ DERGİSİ
ISSN: 2147-3129 / e-ISSN: 2147-3188

EVALUATION OF TEMPERATURE-DEPENDENT VISCOUS DAMPING PERFORMANCE IN A SMART FLUIDIC VIBRATION ISOLATION SYSTEM

Burhan SAHIN [1], **Yasin Furkan GORGULU** [2*]

[1] *Turkish Aerospace Industry, Ankara, Türkiye.*
[2] *Department of Aeronautical Engineering, Eskişehir Osmangazi University, Eskişehir, Türkiye*
**** Corresponding Author:*** *furkan.gorgulu@ogu.edu.tr*

Article Info

Received: *August 3, 2025*
Revised: *December 17, 2025*
Accepted: *January 26, 2026*

Keywords
CFD,
FSI,
Rotorcraft,
Thermal,
Vibration.

ABSTRACT

This study investigates the thermofluidic and structural behavior of a multi-chamber fluidic vibration damping mechanism designed for aerospace applications. A computational fluid dynamics approach, coupled with structural finite element analysis, is employed to evaluate the interaction between pressure-driven flows and material deformation. Four working fluids—Air, Argon, Carbon Dioxide, and Helium—were individually analyzed under a uniform inlet gauge pressure of 200 MPa. The results indicated peak flow velocities exceeding 560 $m.s^{-1}$, localized pressure maxima of 1.01 MPa, and turbulence kinetic energy values surpassing 197,000 $m^2.s^{-2}$, reflecting high internal mixing and energy dissipation. Thermal analysis under convective boundary conditions (15 $W.m^{-2}\cdot K^{-1}$, 280 K ambient) yielded a maximum fluid temperature of 299.7 K. Subsequent structural analyses mapped computational fluid dynamics-derived pressure loads onto three engineering materials: AL 6061-T6, Titanium Ti-6Al-4V, and AISI 316L stainless steel. Although stress levels remained comparable (~36–38 MPa), maximum deformation varied significantly: 0.0102 mm for AL 6061-T6, 0.0065 mm for Ti-6Al-4V, and 0.0043 mm for 316L steel. These findings underscore the critical role of fluid selection and material choice in vibration isolation performance. The integrated fluid-structure interaction simulation framework provides valuable insights for the design and optimization of advanced damping systems in aerospace and energy applications.

1. INTRODUCTION

Pressure-driven fluid systems are integral to various engineering applications, including hydraulic circuits, microfluidic devices, and thermal management systems. These systems rely on pressure differentials to induce fluid motion, and understanding their behavior is crucial for optimizing performance and efficiency. Computational Fluid Dynamics (CFD) has emerged as a powerful tool for analyzing such systems, enabling detailed insights into fluid behavior under varying conditions. The foundation of CFD lies in the governing equations of fluid dynamics—the continuity, momentum, and energy equations—which encapsulate the principles of mass, momentum, and energy conservation, respectively [1]. The energy equation, in particular, plays a pivotal role in capturing the thermal aspects of fluid flow, accounting for heat conduction, convection, and viscous dissipation. In pressure-driven flows, especially those involving significant temperature gradients or viscous effects, incorporating the energy equation is essential for accurate predictions [2]. Recent studies have applied CFD to various pressure-driven systems. For instance, simulations of pressure control valves have elucidated the relationship between flow rate and pressure drop, aiding in the design of more efficient hydraulic components. Similarly, CFD analyses of membrane filtration systems have provided insights into flow distribution and fouling mechanisms, contributing to improved filtration performance [3]. In the realm of microfluidics, pressure-driven flows are commonly employed due to their simplicity and reliability. CFD studies have been instrumental in optimizing microchannel designs to achieve desired flow

characteristics and thermal management [4], [5]. The selection of appropriate turbulence models is another critical aspect of CFD simulations. Models such as k-ε and k-ω SST have been widely used to capture turbulent behaviors in various flow regimes, balancing computational efficiency and accuracy. Moreover, the treatment of pressure-velocity coupling in CFD solvers significantly influences simulation stability and convergence. Algorithms like SIMPLE and PISO have been developed to address these challenges, ensuring accurate pressure field predictions in incompressible flows [6]. Despite these advancements, challenges remain in accurately modeling complex pressure-driven systems, particularly those with intricate geometries or multiphase flows.

Several recent studies have highlighted the importance of understanding temperature and pressure effects on fluid-based vibration damping systems. Zhang et al. investigated the mechanical modeling of viscous fluid dampers under coupled temperature–pressure effects, demonstrating that internal temperature and pressure influence the damping coefficient and energy dissipation, and proposed an improved theoretical model validated against experimental data [7]. This work confirms the necessity of incorporating thermodynamic coupling in damper models, particularly for long-duration dynamic loads. Experimental research by Ye et al. examined the influence of environmental temperature on tuned mass damper performance, showing that temperature variations significantly affect the damping behavior and displacement reduction ratios across a wide range of ambient conditions [8]. Such findings underscore the practical relevance of thermal effects in vibration control devices. A theoretical and numerical study on the thermo-mechanical coupling of fluid viscous dampers developed constitutive models that integrate fluid dynamics and structural response, indicating that temperature-dependent material properties must be considered for accurate performance predictions [9]. The importance of temperature-dependent viscosity on damping efficiency has also been highlighted in studies on viscoelastic materials used in passive damping, illustrating how elevated temperatures reduce energy dissipation capacity [10]. In addition to fluid viscous damper research, broader reviews of viscoelastic damper performance under thermal variations reveal that temperature changes can significantly alter both hysteresis characteristics and structural damping behavior, a trend consistently observed across building and mechanical systems [11]. While these works focus on polymer-based or mechanical dampers, they illuminate the general sensitivity of damping mechanisms to thermal environments. Other investigations have addressed experimental and theoretical aspects of fluid damping. Yang et al. introduced a passive viscous damper with variable performance under different deformation levels, offering insights into geometry-dependent damping. Older but foundational work on viscous heating effects in fluid dampers demonstrated that viscous dissipation can lead to significant temperature rises within damper fluids, affecting force-velocity relationships and energy balance equations [12].

This study aims to enhance the understanding of pressure-driven multi-fluid systems by performing a comprehensive CFD analysis integrated with the energy equation to capture thermal transport phenomena. The modeled configuration features four distinct working fluids confined within independent chambers, allowing the examination of their individual flow and heat transfer behaviors without intermixing. CFD simulations were conducted under realistic pressure boundary conditions, followed by a structural finite element analysis (FEA), where the pressure distributions obtained from the fluid domain were mapped onto the solid components. This fluid–structure interaction (FSI)-informed framework enabled the evaluation of material responses, including stress and deformation, for three engineering alloys-AL 6061-T6, Ti-6Al-4V, and AISI 316L stainless steel. By correlating the pressure, velocity, temperature, and turbulence characteristics with the structural performance under varying thermal and fluidic scenarios, this study provides valuable insights for the design and optimization of thermofluidic vibration damping mechanisms used in aerospace and energy applications [13-17].

2. MATERIALS AND METHODS

2.1. Geometric Configuration and Computational Fluid Dynamics (CFD) Methodology

The fluid-based vibration damping mechanism analyzed in this study is designed to attenuate dynamic loads transmitted through the main rotor and transmission interface in rotary-wing platforms. The system comprises a piston-fluid chamber assembly configured to respond to real-time vibration amplitudes by regulating the distribution of working fluids with different effective stiffness characteristics. This

regulation is controlled by pressure sensors and an electronic processing unit, enabling adaptive damping under varying operational conditions. The geometry includes the hub casing, linear pistons, fluid transmission pipes, and multi-chamber damping reservoirs. CFD simulations were conducted to evaluate the internal fluid behavior and pressure-induced flow dynamics within this configuration under imposed vibrational loading. The vibration damping mechanism in the proposed design is based on internal high-speed fluid motion through multiple chambers with varying cross-sections. As the pressurized fluid flows through these constrictions, localized jet formations and turbulence zones emerge, promoting energy dissipation through momentum and thermal diffusion.

The flow was modeled as a steady-state assuming that transient effects are negligible for the intended vibration damping application. The computational domain was discretized using an unstructured mesh composed of 2,475,894 elements and 920,129 nodes, which provided sufficient spatial resolution for capturing the complex geometry of the multi-chamber fluidic damping system. The computational mesh was generated using unstructured tetrahedral elements for the core flow regions. In order to accurately resolve near-wall velocity and thermal gradients, inflation layers were applied along all solid-fluid interfaces, with a growth rate of 1.2 and a minimum of 5 layers, ensuring adequate resolution of viscous sublayers. Mesh quality was evaluated based on ANSYS Fluent's standard metrics. The average skewness was found to be 0.23125, which lies within the "excellent" range (0–0.25), indicating minimal cell deformation and ensuring accurate numerical interpolation. The orthogonal quality was measured as 0.76746, classified as "very good" (0.70–0.95), which confirms appropriate angular alignment of mesh elements with respect to physical boundaries and gradients [18]. To ensure mesh-independence of the simulation results, a grid convergence study was performed using three mesh densities: coarse (≈1.2 million elements), medium (≈2.4 million elements), and fine (≈4.8 million elements). Key output parameters such as maximum pressure and average velocity at selected monitoring points were compared. Variations between the medium and fine meshes remained below 2%, indicating mesh convergence. As a result, the medium mesh was selected to balance computational cost and solution accuracy. These values collectively demonstrate that the generated mesh offers both numerical stability and geometric fidelity, making it suitable for pressure- and temperature-driven flow simulations in complex internal flow domains. The simulations were performed using the shear stress transport (SST) k-ω turbulence model, which offers robust near-wall treatment and accurate prediction of adverse pressure gradients and separation zones. The energy equation was activated to capture the thermal effects associated with compressible flow and inter-fluid heat transfer. For pressure–velocity coupling, the SIMPLE algorithm was employed, and all spatial discretization was applied using the second-order upwind scheme to ensure numerical accuracy and stability. Four different working fluids were defined using ANSYS Fluent's default materials library: Air, Ar, CO_2, and He. These fluids were selected based on their distinct thermophysical properties, allowing a comparative assessment of pressure distribution, velocity profiles, turbulence intensity, and thermal behavior under identical boundary conditions. The boundary conditions were defined to simulate high-pressure operational conditions relevant to aerospace vibration damping systems. Each of the four fluid inlets was assigned a gauge total pressure of 200 MPa, representing the impulsive force input transmitted through the mechanical system. Outlet boundaries were defined as pressure outlets with a gauge pressure of 0 Pa, enabling free discharge while maintaining numerical stability. All remaining solid-fluid interfaces were treated as no-slip adiabatic walls, assuming negligible heat flux across the boundaries. Convective heat transfer to the ambient was represented using a convection boundary condition with a heat transfer coefficient of 15 $W.m^{-2}.K^{-1}$ and ambient temperature of 280 K, simulating external cooling in low-altitude flight environments. These conditions enabled the representation of extreme thermofluidic environments for performance evaluation, where an inlet pressure of 200 MPa was employed to simulate critical loading scenarios relevant to high-pressure aerospace or hydraulic damping applications, rather than standard operating conditions. The configuration of the multi-chamber fluidic vibration damper, including the allocation of different damping fluids-(a) Air, (b) Argon, (c) Carbon Dioxide, and (d) Helium, from top to bottom, is illustrated in Figure 1. The thermophysical properties of the selected working fluids-Air, Argon (Ar), Carbon Dioxide (CO_2), and Helium (He), used in the CFD simulations are presented in Table 1.

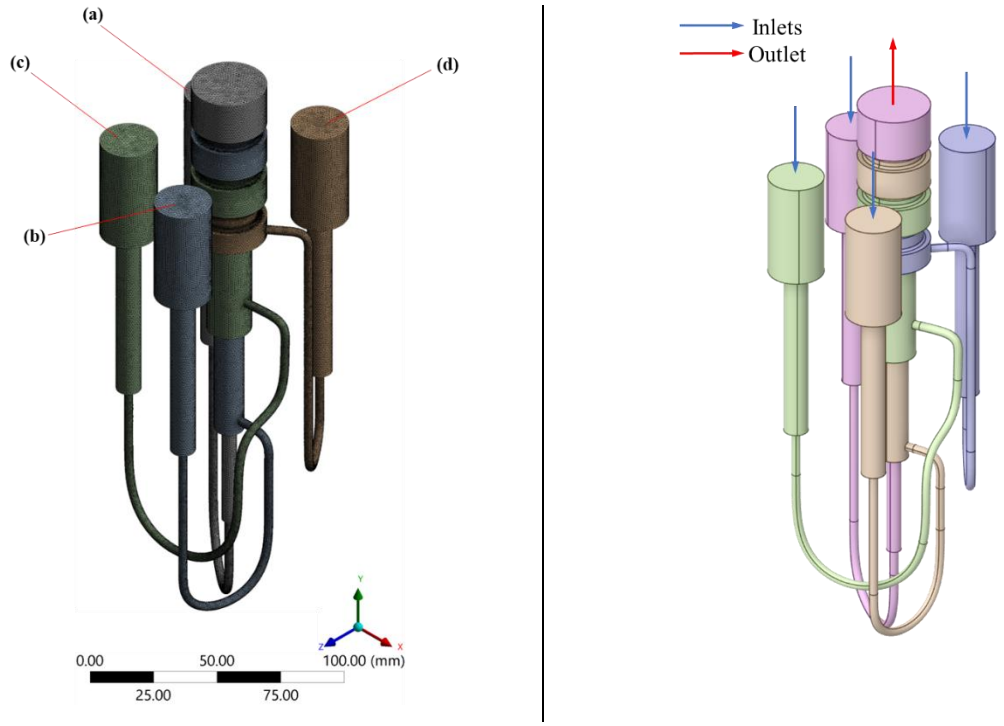

Figure 1. The mesh structure and boundaries of the fluidic vibration damper (a) Air, (b) Argon, (c) Carbon Dioxide, and (d) Helium.

The studied fluidic vibration damping system consists of a multi-chamber configuration, as illustrated in Figure 1. The model includes five cylindrical chambers with different volumes connected through narrow flow channels, forming a closed-loop structure. The geometry was developed as a small-scale prototype to evaluate the feasibility of the damping concept under coupled pressure and thermal loading. The overall height of the system reaches approximately 100 millimeters along the z-axis. The chamber diameters range between 10 and 20 millimeters, while the interconnecting channels exhibit diameters as low as 3 millimeters, resulting in localized flow acceleration. If successful, this compact prototype design is intended to be upscaled and adapted for real-life vibration-sensitive applications, such as aerospace components or high-precision industrial systems. The compact size facilitates detailed CFD and FEA analysis while preserving the essential physical behavior of the system under thermofluidic excitation.

Table 1. Thermophysical properties of working fluids used in the simulations [19], [20], [21], [22].

Property	**Air**	**Ar**	**CO_2**	**He**
Molecular weight [g.mol^{-1}]	28.97	39.95	44.01	4.00
Density [kg.m^{-3}]	1.177	1.784	1.842	0.164
Dynamic viscosity [Pa.s]	1.846×10^{-5}	2.23×10^{-5}	1.48×10^{-5}	1.96×10^{-5}
Thermal conductivity [W.m^{-1}.K^{-1}]	0.0263	0.0177	0.0166	0.1513
Specific heat capacity [J.kg^{-1}.K^{-1}]	1005	520	844	5190
Prandtl number	0.71	0.67	0.74	0.67
Speed of sound [m.s^{-1}]	343	319	259	1007
Kinematic viscosity [m^2.s^{-1}]	1.57×10^{-5}	1.25×10^{-5}	8.03×10^{-6}	1.19×10^{-4}

The simulations were based on the conservation laws for mass, momentum, and energy, which are expressed through the compressible form of the Navier–Stokes equations. The continuity equation

ensures mass conservation within the domain. The momentum equations account for the pressure-driven and viscous forces acting on the fluid. The energy equation incorporates thermal effects, allowing the modeling of temperature variations due to both conduction and convective transport. Turbulent effects were resolved using the shear stress transport k–ω turbulence model. The physical behavior of the compressible gases—Air, Argon, Carbon Dioxide, and Helium, was captured by employing the ideal gas law, which relates pressure, temperature, and density.

2.2. Finite Element Analysis (FEA) and Fluid Structure Interaction (FSI)

In pressure variations and flow analyses, results were simulated based on the 5G pressure level in accordance with the CS.29.561 standard, with each chamber filled to 25% at a pressure of 5MPa. In this region, analyses were conducted using three different materials under 1mm mesh conditions, taking into account a minimum wall thickness of 3mm [23]. The design software utilized was NX 21, while the analysis was performed using Ansys Fluent 2022 R2, focusing on static analysis. The pump area was separated from other equipment and modeled with its chambers, with materials assigned as a complete unit. The properties of the materials are given in Table 2.

Table 2. Materials of main body of construction [24], [25], [26], [27].

Material	Modulus of Elasticity [GPa]	Poisson Ratio	Density [kg.m^{-3}]	Tensile Yield Strength [MPa]
AL 6061 T6	68.9	0.33	2700	276
Titanium Ti-6Al-4V	113.8	0.342	4430	880
AISI Type 316L Stainless Steel	193	0.3	8000	515

3. RESULTS AND DISCUSSION

Figure 2 presents the contour distributions for the selected physical quantities within the fluidic vibration damping mechanism:

(a) Temperature [K],

(b) Pressure [Pa],

(c) Velocity magnitude [m·s^{-1}], and

(d) Turbulence kinetic energy [m²·s^{-2}].

The temperature distribution (Figure 2a) illustrates a gradual thermal gradient from the bottom of the system to the top, consistent with the applied convection boundary condition of 15 W·m^{-2}·K^{-1} and ambient temperature of 280 K. Maximum temperatures approaching 299.7 K were observed in the upper chambers, which are located near the heat-accumulating zones. The narrow fluid conduits show slightly lower temperatures, likely due to increased convective heat dissipation and limited residence time for thermal energy transfer. This confirms that thermal stratification develops along the vertical axis, and the fluid movement supports upward thermal transport.

The pressure field (Figure 2b) reveals significant pressure gradients throughout the system. A maximum gauge pressure of approximately 1.01 MPa is recorded at the primary inlet, gradually dropping along the channels due to viscous and inertial losses. Localized pressure drops occur at sharp bends and junctions, which may induce flow separation or secondary vortices. These results demonstrate the capability of the structure to distribute the applied input pressure effectively across the multi-chamber damping network, which is essential for fluid-based vibration attenuation.

The velocity magnitude contour (Figure 2c) exhibits high-speed jet formation in narrow regions, with peak velocities exceeding 560 m.s^{-1} in the upper sections where cross-sectional contraction accelerates flow. In the narrow upper chambers where jet acceleration occurs, peak flow velocities slightly exceed the local speed of sound, indicating localized supersonic conditions. To ensure numerical stability and accurate resolution of compressibility effects and potential shocks, the density-based solver in Ansys

Fluent was employed with appropriate shock-capturing capabilities. The SST k-ω turbulence model, along with energy equations and compressible flow formulation, enabled the resolution of high-speed gradients and shock layers without requiring additional artificial stabilization or flux limiters. The broader chambers show significantly lower flow velocities, indicating energy dissipation and potential stagnation regions. This variation confirms that the geometry effectively introduces pressure and velocity decoupling zones, essential for dynamic damping. Additionally, flow asymmetry suggests the formation of directional circulation patterns within the chambers.

Figure 2d illustrates the distribution of turbulence kinetic energy (TKE) within the system. Peak values surpass 197000 $m^2.s^{-2}$, especially around inlet regions and sudden expansions or contractions in the geometry. These high-TKE regions align with zones of intense shear and recirculation, which contribute to dissipating mechanical energy into heat. The increased turbulence in specific fluid paths suggests effective momentum exchange, an important characteristic for dissipative vibration control. On the other hand, regions with low TKE indicate laminar or stabilized flows, particularly in vertically aligned conduits.

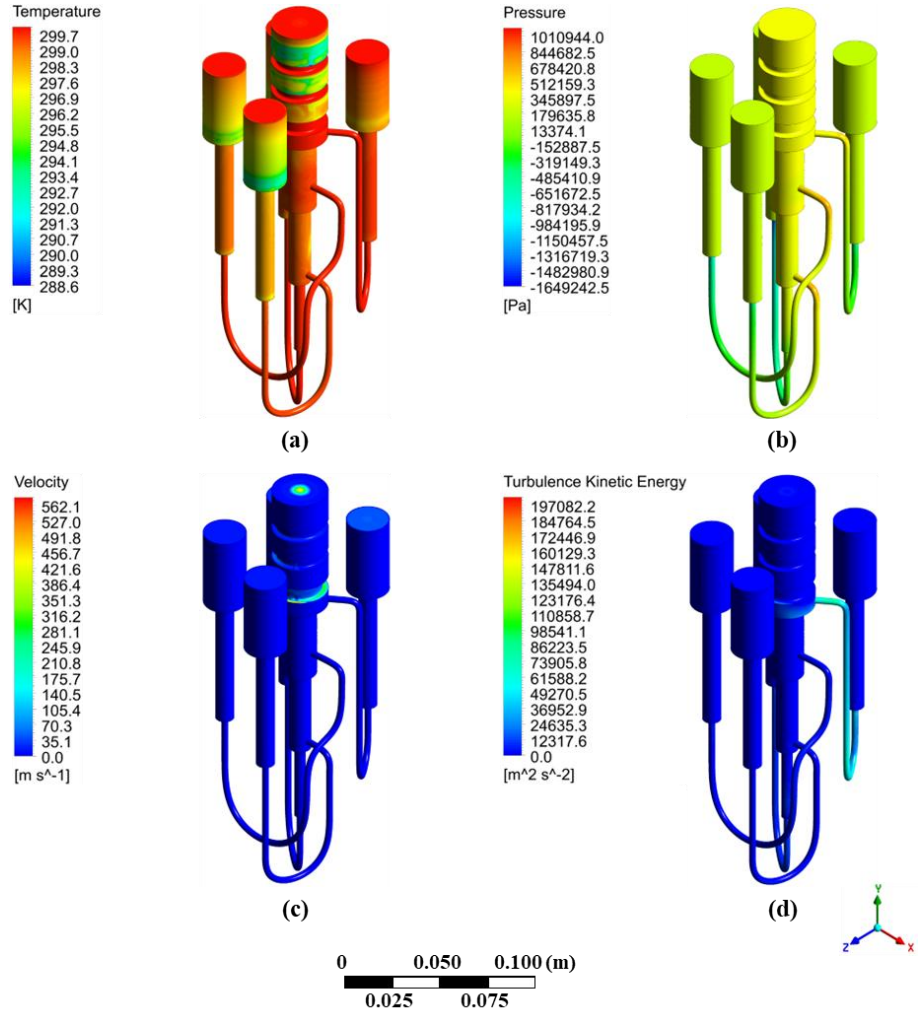

Figure 2. CFD contour results for the fluidic vibration damper: (a) temperature, (b) pressure, (c) velocity, and (d) turbulence kinetic energy distributions.

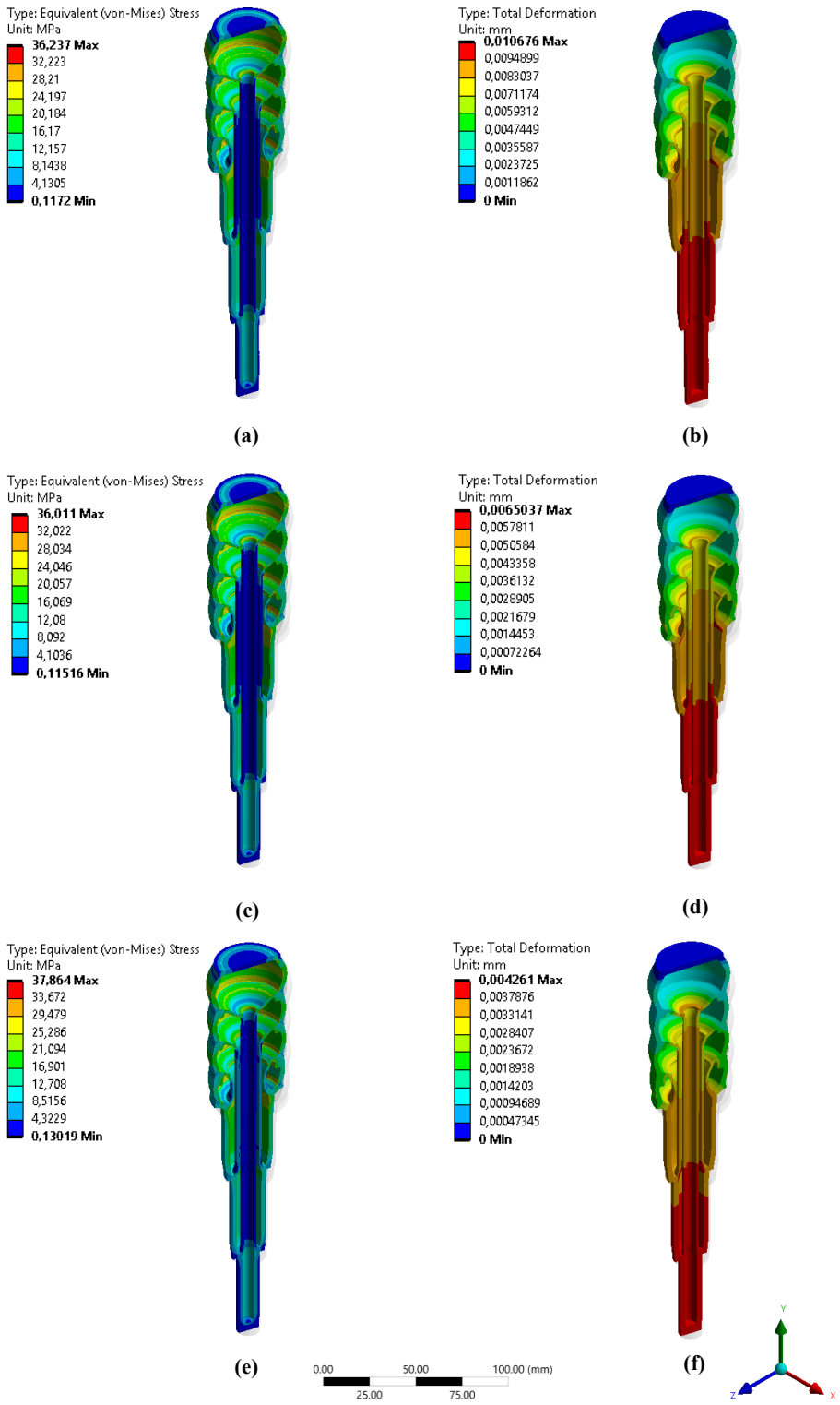

Figure 3. Structural analysis results of the vibration damping mechanism under CFD-derived pressure loads for three different materials: (a) von Mises stress distribution for AL 6061-T6, (b) total deformation of AL 6061-T6, (c) von Mises stress distribution for Titanium Ti-6Al-4V, (d) total deformation of Titanium Ti-6Al-4V, (e) von Mises stress distribution for AISI 316L Stainless Steel, (f) total deformation of AISI 316L Stainless Steel.

Following the pressure contour results obtained from the CFD simulations, structural analyses were performed on the vibration damping mechanism using three distinct engineering materials: AL 6061-T6, Titanium Ti-6Al-4V, and AISI 316L Stainless Steel. Each material was subjected to the same

pressure distribution profiles, with equivalent von Mises stress and total deformation fields extracted for evaluation. Figure 3. presents the results as follows:

(a–b) AL 6061-T6,

(c–d) Titanium Ti-6Al-4V,

(e–f) AISI 316L Stainless Steel.

This aluminum alloy exhibited a maximum von Mises stress of 36.24 MPa and a total deformation of 0.010176 mm. Despite its relatively low Young's modulus, AL 6061-T6 demonstrates acceptable stress resistance, though its higher deformation suggests a limited capacity for maintaining dimensional stability under continuous vibrational loads. The titanium alloy showed a comparable stress magnitude (36.01 MPa) but with a much lower deformation of 0.0065037 mm, confirming its high stiffness and strength-to-weight ratio. These results emphasize the material's excellent structural resilience, making it highly suitable for critical aerospace damping applications. While exhibiting the highest equivalent stress (37.86 MPa), the deformation was found to be the lowest among the three materials at 0.004261 mm. This indicates that AISI 316L provides superior rigidity under the same loading conditions, but at the expense of increased mass, which may affect system dynamics in airborne applications. Despite minor variations in maximum stress values (all remaining below typical yield thresholds), the choice of material significantly influences deformation behavior. Titanium offers a balance between low deformation and moderate weight, while stainless steel maximizes stiffness at the cost of mass. Aluminum provides a lightweight solution but may be prone to larger structural deflections. The selection thus depends on application priorities—whether weight reduction, rigidity, or fatigue resistance is paramount. According to the results obtained, the deformation rates for all three materials appear to be safe up to four times the standard NC production thickness of 3mm. Structural design load analyses should account for dynamic environments including quasi-static and transient acceleration effects. In spacecraft mechanical loads analysis practice the European Cooperation for Space Standardization provides guidelines for mechanical loads and dynamic environments, which engineers use to establish appropriate loads for preliminary design and verification consistent with these environments. According to the ECSS-E-HB-32-26A handbook, spacecraft loads analysis methodology includes dynamic loads and their contribution to design limit loads. This rationale supports using a design acceleration limit such as 20 G for preliminary structural sizing under combined static and dynamic loads [28]. The standard materials and pipes utilized will also be selected for this pressure level. The fact that the deformation and stress values remain at this level even under maximum pressure will not only provide an advantage for vibration but will also minimize the factors contributing to heat generation due to friction.

The integrated CFD and structural analysis provided a holistic understanding of the thermofluidic performance and mechanical resilience of the proposed vibration damping mechanism under high-pressure, multi-fluid loading conditions. The CFD simulations revealed spatial variations in pressure, temperature, velocity, and turbulence across the complex geometry, which directly influenced the structural stress and deformation responses. High-pressure regions identified near the fluid inlets, with peak gauge pressures exceeding 1.01 MPa, acted as primary loading zones in the structural domain. These localized peaks, along with directional flow asymmetries and high-velocity jets (up to 560 $m.s^{-1}$), contributed to elevated turbulence kinetic energy (TKE > 197,000 $m^2.s^{-2}$), indicating intense momentum exchange and energy dissipation. The thermal analysis indicated stratified heat transfer behavior, with maximum temperatures near 299.7 K occurring in upper chamber zones due to convective accumulation. These temperature fields, though modest in magnitude, informed the application of temperature-dependent material properties in the subsequent structural simulations. The pressure contours were mapped onto the solid domain for each of the three candidate materials, resulting in von Mises stress and total deformation evaluations. Despite similar stress levels (~36–38 MPa), notable differences in deformation responses were observed: AISI 316L exhibited the highest stiffness (lowest deformation), whereas AL 6061-T6, while lighter, experienced greater deflection. Titanium Ti-6Al-4V provided a favorable balance with low deformation and moderate weight, underscoring its suitability for airborne damping systems. Collectively, these results highlight the critical interplay between internal fluid dynamics and external structural stability, particularly in aerospace environments subject to vibrational

and thermal loads. The proposed fluidic damper demonstrated effective attenuation capacity by leveraging the distinct thermophysical characteristics of the working fluids and the mechanical integrity of carefully selected materials. These insights offer valuable design guidance for future implementations of smart FSI-based vibration isolation systems in rotorcraft and high-performance energy platforms.

4. CONCLUSION

This study presented a CFD and FSI-integrated structural analysis of a fluid-based vibration damping mechanism tailored for aerospace platforms. The analysis involved four different working fluids-Air, Argon, Carbon Dioxide, and Helium, under extreme inlet pressure conditions of 200 MPa to replicate the dynamic loads typical in rotorcraft systems. The methodology enabled the evaluation of both fluid dynamics and structural responses within a unified simulation environment.

The key findings of the study are summarized as follows:

- Maximum pressure values exceeding 1.01 MPa were observed near the inlet zones, indicating high fluid impingement regions.
- The peak velocity magnitude reached approximately 560 $m \cdot s^{-1}$, confirming the development of high-momentum jets through the narrow passages.
- Turbulent kinetic energy peaked at 197,000 $m^2 \cdot s^{-2}$, highlighting significant internal mixing and energy dissipation within the chambers.
- Maximum fluid temperature rise was limited to 299.7 K, under ambient conditions of 280 K and convective heat transfer coefficient of 15 $W \cdot m^{-2} \cdot K^{-1}$.
- All materials maintained von Mises stress values around 36–38 MPa, well below yield limits, while deformation differed significantly:
    - AL 6061-T6: 0.0102 mm
    - Titanium Ti-6Al-4V: 0.0065 mm
    - AISI 316L Stainless Steel: 0.0043 mm
- The integration of CFD and structural solvers provided accurate pressure-to-deformation mapping, enabling more reliable design evaluation under multiphysics loading.

Overall, the proposed multi-fluid, pressure-driven damping configuration exhibits potential as a lightweight and adaptive solution for aerospace vibration control. The results demonstrate that selection of working fluid and structural material can significantly influence the damping efficiency. The methodology established in this study may serve as a foundational framework for the future design of smart, thermofluidically responsive damping systems.

Acknowledgements

The authors declare that they have no conflict of interest. Also, this research did not receive any specific grant from funding agencies in the public, commercial, or not-for-profit sectors.

Conflict of Interest Statement

There is no conflict of interest between the authors.

Statement of Research and Publication Ethics

The study is complied with research and publication ethics.

Artificial Intelligence (AI) Contribution Statement

This manuscript was written and edited by the authors. ChatGPT was only utilized for minor language proofreading to enhance clarity and fluency. No AI tools were used for data analysis, figure generation, or content creation.

Contributions of the Authors

Burhan SAHIN: Conceptualization, Methodology, Software, Validation, Resources, Data Curation, Writing - Original Draft, Writing - Review & Editing, Visualization, Funding acquisition.

Yasin Furkan GORGULU: Conceptualization, Methodology, Software, Validation, Formal analysis, Investigation, Data Curation, Writing - Original Draft, Writing - Review & Editing, Visualization, Supervision, Project administration.

REFERENCES

[1] J. D. Anderson, "Governing Equations of Fluid Dynamics," in *Computational Fluid Dynamics*, Berlin, Heidelberg: Springer Berlin Heidelberg, 1992, pp. 15–51. doi: 10.1007/978-3-662-11350-9_2.

[2] G. Keir and V. Jegatheesan, "A review of computational fluid dynamics applications in pressure-driven membrane filtration," *Rev. Environ. Sci. Bio/Technology*, vol. 13, no. 2, pp. 183–201, Jun. 2014, doi: 10.1007/s11157-013-9327-x.

[3] D. Wu, S. Li, and P. Wu, "CFD simulation of flow-pressure characteristics of a pressure control valve for automotive fuel supply system," *Energy Convers. Manag.*, vol. 101, pp. 658–665, 2015, doi: 10.1016/j.enconman.2015.06.025.

[4] M. H. Chaudhry, *Open-Channel Flow*. Boston, MA: Springer US, 2008. doi: 10.1007/978-0-387-68648-6.

[5] F. White and J. Majdalani, *Viscous Fluid Flow*, 4th ed. McGraw-Hill, 2022.

[6] J. Wright and S. Thakur, "Development of a Pressure-Based CFD Solver for All-Speed Flows on Arbitrary Polygonal Meshes in a Rule-Based Framework," in *Thermal and Fluids Analysis Workshop (TFAWSO3)*, 2003, pp. 1–16.

[7] Y. Zhang, W. Xu, S. Wang, D. Du, and Y. Geng, "Mechanical Modeling of Viscous Fluid Damper with Temperature and Pressure Coupling Effects," *Machines*, vol. 12, no. 6, p. 366, May 2024, doi: 10.3390/machines12060366.

[8] D. Ye, J. Tan, Y. Liang, and Q. Feng, "Experimental Study on Influence of Temperature to Control Performance for Viscoelastic Materials Pounding Tuned Mass Damper," *Front. Mater.*, vol. 8, May 2021, doi: 10.3389/fmats.2021.676405.

[9] S. Hu, H. Hao, D. Meng, and M. Yang, "Theoretical and numerical study of the thermo-mechanical coupling effect on the fluid viscous damper," *J. Sound Vib.*, vol. 597, p. 118846, Feb. 2025, doi: 10.1016/j.jsv.2024.118846.

[10] L. Witek and P. Łabuński, "Influence of Temperature on the Damping Properties of Selected Viscoelastic Materials," *Materials (Basel).*, vol. 17, no. 23, p. 5832, Nov. 2024, doi: 10.3390/ma17235832.

[11] Y. Liu, "A review of the effect of temperature on the performance of viscoelastic dampers," *J. Phys. Conf. Ser.*, vol. 2798, no. 1, p. 012041, Jul. 2024, doi: 10.1088/1742-6596/2798/1/012041.

[12] C. J. Black and N. Makris, "Viscous heating of fluid dampers: experimental studies," in *7th International Symposium on Smart Structures and Materials*, T. T. Hyde, Ed., Apr. 2000, pp. 256–265. doi: 10.1117/12.384566.

[13] S. Miao, J. Ma, X. Zhou, Y. Zhang, and H. Chu, "A review of CFD simulation in pressure driven membrane with fouling model and anti-fouling strategy," *Front. Environ. Sci. Eng.*, vol. 18, no. 8, p. 93, Aug. 2024, doi: 10.1007/s11783-024-1853-y.

[14] M. Domagala and J. Fabis-Domagala, "A Review of the CFD Method in the Modeling of Flow Forces," *Energies*, vol. 16, no. 16, p. 6059, Aug. 2023, doi: 10.3390/en16166059.

[15] C. De Michele and G. Coppola, "Numerical treatment of the energy equation in compressible flows simulations," *Comput. Fluids*, vol. 250, p. 105709, Jan. 2023, doi: 10.1016/j.compfluid.2022.105709.

[16] K. Ali, W. Jamshed, S. Suriya Uma Devi, R. W. Ibrahim, S. Ahmad, and E. S. M. Tag El Din, "A study of pressure-driven flow in a vertical duct near two current-carrying wires using finite volume technique," *Sci. Rep.*, vol. 12, no. 1, p. 21273, Dec. 2022, doi: 10.1038/s41598-022-25756-4.

[17] F. Marchelli, L. Fiori, and R. Di Felice, "Cohesive particle–fluid systems: An overview of their CFD simulation," *Can. J. Chem. Eng.*, vol. 103, no. 4, pp. 1582–1601, Apr. 2025, doi: 10.1002/cjce.25269.

[18] Y. F. Gorgulu, "Thermal efficiency evaluation in shell-and-tube heat exchangers: A CFD-based parametric study," *Proc. Inst. Mech. Eng. Part E J. Process Mech. Eng.*, 2024, doi: 10.1177/09544089241262481.

[19] Y. A. Çengel and M. A. Boles, *Thermodynamics: An Engineering Approach*, 8th ed. McGraw-Hill, 2015.

[20] T. L. Bergman, A. S. Lavine, F. P. Incropera, and D. P. DeWitt, *Fundamentals of Heat and Mass Transfer*, 7th ed. Jefferson City, USA: Wiley, 2011.

[21] National Institute of Standards and Technology (NIST), "Chemistry WebBook." Accessed: Aug. 03, 2025. [Online]. Available: https://webbook.nist.gov/

[22] F. M. White, *Fluid Mechanics*, 8th ed. New York: McGraw-Hill, 2015.

[23] ASME, "ASME boiler and pressure vessel code. American Society of Mechanical Engineers," 1989.

[24] ASM Aerospace Specifications Metals Inc., "Material Data Sheet." Accessed: Aug. 02, 2025. [Online]. Available: https://asm.matweb.com/search/specificmaterial.asp?bassnum=ma6061t6

[25] J. M. (Tim) Holt, *Structural Alloys Handbook*. West Lafayette: CINDAS/Purdue University, 1996.

[26] ASM International, *ASM Handbook Volume 2: Properties and Selection: Nonferrous Alloys and Special-Purpose Materials*, 10th ed. ASM International, 1990.

[27] H. E. Boyer and T. L. Gall, *Metals Handbook*. ASM International, 1985.

[28] European Cooperation For Space Standardization, "Spacecraft mechanical loads analysis handbook," Noordwijk, 2013.